

## Constriction Flow of Cellulose Laden Air-Aqueous Foam

Leevi Viitanen,\* Alisa Halonen, Eira Friström, Juha Koivisto, Marko Korhonen, Antti Puisto, and Mikko Alava

Foams are encountered in everyday life across wide applications, e.g., in foods and cleaning products. They have also been widely used in different industries in processes such as flotation and oil recovery. The application of bio-based materials is a novel interest, and foam forming enables these materials to be used more flexibly. For efficient industrial usage, the flow of such materials must be well understood and characterized. This work measured the velocity field of nanocellulose laden foam in a two-dimensional Hele-Shaw cell with a constriction, using optical imaging and particle image velocimetry. The measurements showed that the addition of cellulose increased the effective viscosity of the liquid films. In a numerical simulation using the Giesekus polymer model, the experimental trend was reproduced through increasing the fluid's viscosity. Adding highly viscoelastic nanofibrillated cellulose suspension to foam affected only the viscous component of the foam. The delayed elastic response did not change.

*Keywords:* Foam; Microfibrillated cellulose; Hele-Shaw; Rheology; Foam forming; Giesekus model

*Contact information:* Department of Applied Physics, Aalto University School of Science, P.O. Box 11100, FI-00076 AALTO, Espoo, Finland; \*Corresponding author: leevi.viitanen@aalto.fi

### INTRODUCTION

There has been a continuous search for new sustainable materials to replace their fossil-based counterparts. Wood, being a renewable raw material, is an attractive source material for these new products. Foam forming technologies have made it possible to produce such new materials (Al-Qararah *et al.* 2015). An example is in paper production, where foam could be used to replace water to improve the efficiency of the forming process, resulting in good-quality end products (Koponen *et al.* 2016). The current paper making technique results in an anisotropic end product where the alignment of the fibers favor the direction of the movement of the forming fabric during the papermaking process (Alava and Niskanen 2006). In foam forming, cellulose fibers are embedded in a foam, preserving the structure formed by the fibers until the pulp reaches the forming fabric of a paper machine (Lappalainen *et al.* 2014). Achieving a homogeneous quality of the end product, by means of foam forming, requires knowledge of behavior of the bubbles on the paper machine forming fabric. The foam forming method also reduces problems caused by flocculation (Gatward and Radvan 1973), and gives a better efficiency compared to wet forming due to reduced drying costs. Unfortunately, this comes at the cost of weaker mechanical properties such as strength and bending resistance, reducing the methods attractiveness in papermaking (Kinnunen-Raudaskoski 2017). Also, generating the bubbles for the process is challenging. However, despite the fact that it was originally developed for papermaking, the foam forming process has a huge potential to widen the application window of cellulosic materials beyond paper by extending the accessible space of end structures and raw materials. In addition to paper, foam forming technology enables

manufacturing of new products to replace plastics with biodegradable materials. Existing examples are for instance fiber sheets that can replace plastic bags (Torniainen *et al.* 2017) and light weight fibrous material to replace polystyrene products (Kiiskinen *et al.* 2016). As foam is a complex fluid, the change in the flow behavior when cellulose fibers are added is non-trivial and needs to be studied, and thus is one of the focus points of this article.

Liquid foams consist of gas bubbles that are separated from each other by thin liquid films. They are characterized as yield stress fluids that respond elastically to small stresses due to their structure (Guillermic *et al.* 2013). The rheology of steadily sheared foams is often described using the Herschel-Bulkely constitutive equation (Eq. 1),

$$\tau = \tau_y + k \times \dot{\gamma}^n \quad (1)$$

where  $\tau$  is the shear stress,  $\tau_y$  is the yield stress,  $\dot{\gamma}$  is shear rate, and the coefficients  $n$  and  $k$  are called the flow index and the consistency, respectively (Denkov *et al.* 2012; Cohen-Addad *et al.* 2013). Based on Eq. 1 (Herschel-Bulkley equation), an effective viscosity is defined as the ratio of shear stress and shear rate,

$$\eta_{\text{eff}}(\dot{\gamma}) = \frac{\tau_y + k \times \dot{\gamma}^n}{\dot{\gamma}} \quad (2)$$

where, because of the finite yield stress, viscosity diverges as the shear rate approaches zero (Møller *et al.* 2006). The Herschel-Bulkely law describes the steady flow of a complex fluid.

However, a flow may have a time-dependent behavior that is amplified by the viscoelasticity of the fluid. The Herschel-Bulkley model does not account for this behavior. Such effects are readily observed in more complex geometries, such as the widely studied geometry of a foam flow in a channel past an obstacle. There, the time-dependent behavior emanating from viscoelasticity is observed as a local velocity maximum that has been detected behind the obstacle using experiments both in two-dimensional (2D) (Dollet *et al.* 2005; Dollet and Graner 2007; Raufaste *et al.* 2007; Chevalier *et al.* 2017) and three-dimensional (3D) approaches (Raufaste *et al.* 2015). The catalyst for such an experiment is the seminal work from the 1970s when bubbles rising in polymer solutions were found to have a ‘wake’, where the flow points away from the obstacle (Hassager 1979).

Additionally, the geometry can be inverted. When constriction geometry is used, the channel has a wall with a narrow opening (see Fig. 1). Earlier study of foam flow in this geometry has found a local velocity minimum, or undershoot, past the constriction (Dollet 2010). Previously, various constriction geometries have been studied in experiments and simulations (Jones *et al.* 2011; Jones and Cox 2012). In addition, a meso-scale bubble model has been utilized to study the impact of the foam flow rate on the flow through the constriction (Langlois 2014).

Understanding the behavior of particle-laden foams during processing is essential for manufacturing advanced structures from novel environmentally friendly materials; for instance, foam forming of wood-based fibers into biocomposites. Therefore, the aim of the present article is to study the influence of nanofibrillated cellulose (NFC) on foam flow at different cellulose concentrations in a flow geometry that imposes unsteady flow. The undershoot detected in the constriction flow (Dollet 2010) was used as the characteristic feature of the foam’s time dependent elastic properties. To comprehend the experimental data, the experiments were compared to the simulation results of viscoelastic flow through constriction that were obtained using the Giesekus model.

## EXPERIMENTAL

### Materials

#### *Foam composition and preparation*

The bubbles were generated to form foam by flowing gas in the liquid solution through a syringe needle. The air injection needle was located in the inlet pipe roughly 5 cm from the cell, allowing the foam to enter the Hele-Shaw cell almost immediately after its production. The liquid solution consisted of water and Fairy dish washing soap (Procter & Gamble, Cincinnati, OH, USA), which contains surface tension decreasing surfactant molecules such as sodium dodecyl sulfate (SDS) and sodium laureth sulfate (SLES). The mass fraction of Fairy in the liquid solution was 2.5 wt%. The foam rheology was changed by adding microfibrillated cellulose made from commercial Birch BHWK bale pulp (UPM, Espoo, Finland) to the liquid solution. To prepare the MFC, the cell wall is deconstructed in enzymatic hydrolysis process using Ecopulp R (AB enzymes) 1.5 mg/g. In the preparation process the pulp is mixed in a high power mixer for 2 hours with the enzyme. This reduces the average fiber length from 1 mm to 0.2 mm. Four microfibrillated cellulose concentrations were used in the liquid solution. The concentrations were 0.0 wt%, 1.0 wt%, 2.0 wt%, and 4.0 wt%. All experiments and sample preparations were performed in room temperature  $T = 22 \pm 1$  °C.

#### *Measurement setup and sample material*

The foam was injected into the Hele-Shaw cell through an inlet as shown in Fig. 1. In the middle of the channel, the foam flowed through a constriction. The experiments were performed in two separate measurement sets.

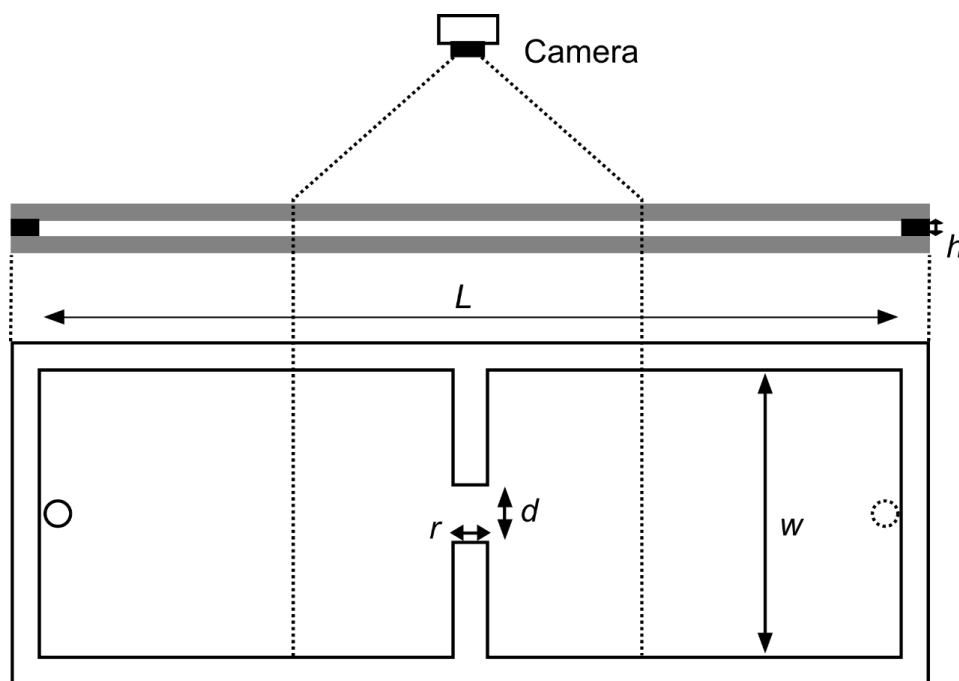


**Fig. 1.** The Hele-Shaw cell was comprised of two acrylic plates with sealed edges. The channel length was  $L$  and the width was  $w$ . Constriction was at the middle of the channel and it had length  $r$  and width  $d$ . The foam was inserted through the inlet hole on the left (solid circle) and flowed out from the outlet at the right (dotted circle). A camera above the device recorded videos of the flow around the constriction.

In the first set of exploratory nature, a constant driving pressure was maintained and microfibrillated cellulose was used. In the second set, the initial flow velocity was kept constant by adjusting the driving pressure according to the nanofibrillated cellulose concentration. Aqueous (nano)fibrillated cellulose solutions are highly viscous due to the high aspect ratio of the fibers even at low mass concentrations (Puisto *et al.* 2012). We expect to see similar behavior in NFC laden foams as well even in the presence of surfactants.

The pressure-controlled experiment was exploratory in nature, during which the hypothesis that cellulose merely affects the effective viscosity was first studied. The flow-controlled experiment and simulations were then performed more thoroughly. The typical bubble radius was approximately  $r_b = 5$  mm. The channel was wide enough for dozens of bubbles to pass through with negligible boundary effects, while the gap was small enough to generate a significant increase in the flow velocity.

#### *Constant pressure*

In the first set, where a constant pressure was maintained, the channel length was  $L = 570$  mm, and the width was  $w = 350$  mm. The height of the cell was  $h = 3$  mm. The foam was inserted into the system through a single inlet at one edge and was allowed to exit through an outlet on the other edge of the channel. The constriction in the middle of the channel was made of two walls at each side of the channel. The constriction wall thickness was  $r = 15$  mm and the channel width at the constriction was  $d = 30$  mm.

#### *Constant velocity*

The measurement setup was slightly modified in the second measurement set. The channel length was  $L = 860$  mm and the width was  $w = 180$  mm. The longer channel ensured the relaxation to homogeneous flow downstream of the constriction. The constriction length was  $r = 20$  mm, and the width was  $d = 20$  mm. The gap between the acrylic plates was  $h = 2.25$  mm. Again, the foam was administered to the channel *via* the inlet pipe. However, the driving pressure was varied with cellulose concentration to ensure constant foam velocity between experiments.

The foam was made by injecting pressured air into a liquid soap solution through a syringe needle, as was done in the previous measurement set. The flow properties of the foam were altered *via* the addition of cellulose. The cellulose product, used in the second set of experiments, was Biofibrilis (UPM-Kymmene, Espoo, Finland), which consists of cellulose fibrils that were obtained from wood-based pulp and have a length of several micrometers and a diameter that ranges between 4 nm and 50 nm. The cellulose concentrations used were 0 wt%, 0.25 wt%, and 0.5 wt%. Smaller concentrations were required as this cellulose product had a stronger impact on the flow properties of the liquid solution in small concentrations. With a liquid fraction  $\phi = 3.6 \pm 0.2$  vol% (see Table 1), the overall density of the cellulose laden sample foam was  $\rho = 36 \pm 2$  kg/m<sup>3</sup>.

A further enhancement over the pressure-controlled experiments was achieved by verifying that the cellulose concentration was the only varying parameter in the experiments. The liquid fraction  $\phi$  was also determined for each sample. The liquid fractions for each case are reported in Table 1. Previous studies have indicated that changing the liquid fraction changes the properties of foam, including the contact number  $Z$  (Katgert and Van Hecke 2010), the yield stress, storage, and loss moduli (Saint-Jalmes and Durian 1999). The radical change in properties, known as (un)jamming transition (Liu and Nagel 1998) where the bubbles lose contact resulting in a loss of rigidity, occurs at

critical liquid fraction close to  $\phi_C \approx 16$  vol% for quasi 2D foams (O'Hern *et al.* 2003; Van Hecke 2009). As shown in Table 1, the liquid fractions were safely below the critical value, and considering the errors of the values for  $\phi$ , were essentially the same.

**Table 1.** Liquid Fractions  $\phi$  Collected for Experiments with Different Cellulose Concentrations C

C (wt%)	0.0	0.25	0.5
$\phi$ (vol%)	$3.6 \pm 0.3$	$3.6 \pm 0.2$	$3.1 \pm 0.4$

## Methods

The flow field was determined from videos recorded with a regular digital camera. The camera was a Canon EOS M3 equipped with a Canon EF 75-300 mm lens (Canon, Tokyo, Japan). The camera recorded videos with a frame rate of 25 frames per second (fps). However, when the videos were coded to sequences of images, the frame rate was dropped to 10 fps to 15 fps. The authors have verified that changing the frame rate within this interval did not alter the obtained flow field.

The extracted frames were analyzed using digital particle image velocimetry (DPIV) (Thielicke and Stamhuis 2014). Through using the DPIV technique to obtain the displacement of each point in the images between frames, subsequent images were cross-correlated. Using the displacement field made it possible to calculate the velocity field between two frames using the frame rate. The reported velocity field was the temporal average over a single experiment. The field close to the constriction was of particular interest; thus, the  $x$ -component of the velocity vector  $u$  that was parallel to the flow at the center axis was examined.

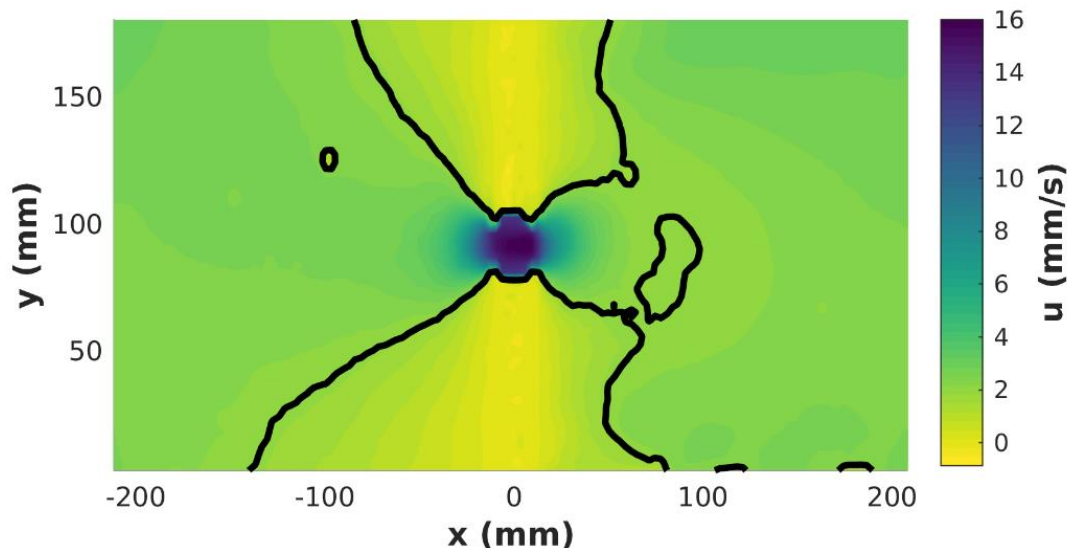


**Fig. 2.** The contour plot of the spatial velocity  $x$ -component shows the negative wake past the constriction. The color indicates the velocity  $x$ -component as indicated by the color bar on the right. The center of the constriction was at  $x = 0$  mm. The black solid line is the contour line  $u = 1.92$  mm/s. The area around  $x = 80$  mm and  $y = 80$  mm, isolated by the contour line, is a local minimum known as the undershoot, which is found in constriction flow of viscoelastic fluids.

## RESULTS AND DISCUSSION

An example of the measured flow fields near the constriction is displayed in Fig. 2. The symmetry before and after the constriction was broken, as shown in a previous study (Dollet 2010). A clear indication of the symmetry being broken was the undershoot that was found past the constriction. The local velocity minimum, indicated as an isolated area with the solid line, is the undershoot. On a Newtonian fluid one would expect an increase of the flow rate at the symmetry axis on  $y = 80$  mm at the constriction and the flow field would be either at or above the driving velocity. However, Fig. 2 shows velocities that are lower than the driving velocity, highlighted as a constant contour line, creating an undershoot around  $x = 80$  and  $y = 80$  mm. This indicates that the studied foam was not Newtonian and can store elastic energy.

Next, the effect of cellulose concentration on the foam flow at the center line  $y = 80$  mm was studied. For this purpose, the velocity profiles were drawn for various cellulose concentrations. The results of the experiments that were based on constant pressure and constant velocity were considered separately.

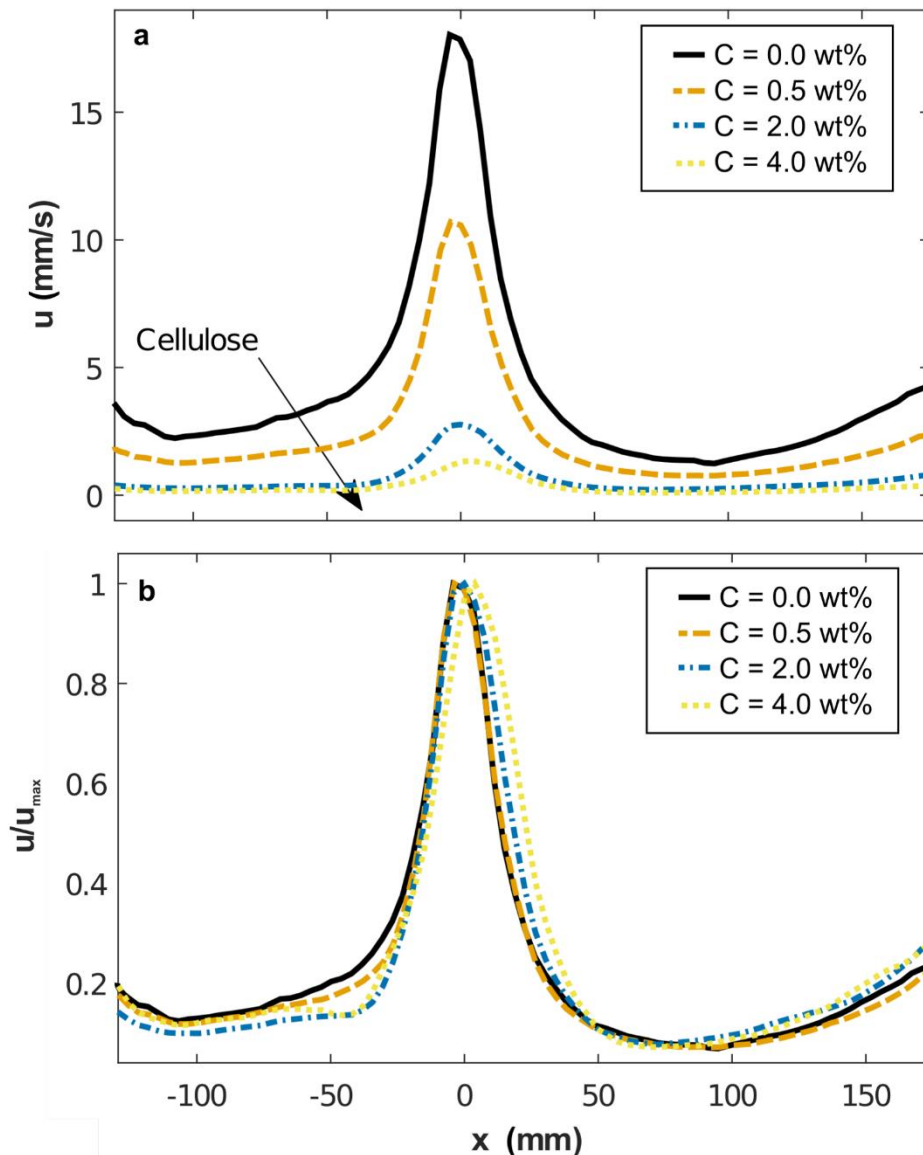
### Constant Pressure Experiments

Figure 3 shows the velocity profile at the center line of the cell for four different foams with cellulose concentrations 0.0 wt%, 0.5 wt%, 2.0 wt%, and 4.0 wt%. Figure 3a shows that the overall flow resistance of the system increased with the cellulose concentration. In contrast, Fig. 2 shows a plug flow at the constriction and that the volumetric flow rate can be estimated from the center line. The flow resistance of the cell increased because the flow rate dropped while the driving pressure remained constant. Thus, it was observed that the effective dissipation increased. With the cellulose concentrations  $C = 0.0$  wt% and  $C = 0.5$  wt%, the velocity displayed an undershoot after the constriction. For the case with a higher value for  $C$ , it was hard to tell whether an undershoot existed. Additionally, comparing the magnitude of the undershoots was impossible based on Fig. 3a.

In Fig. 3b, the velocities are scaled by the maximum velocity at the center of the constriction  $u_{max}$  to compare the experiments at different concentrations. The velocity undershoot appeared in the curves for all of the concentrations, and the scaled velocities had similar shapes. Overall scaling with  $u_{max}$  collapses the velocity curves in agreement with earlier simulations and experiments, where a collapse was found regardless of the constriction shape (Jones and Cox 2012) or driving pressure (Langlois 2014) used. However, there were a few subtle differences. The decrease of cellulose shifted the peak velocity to the left, in the negative  $x$ -direction. In contrast, the minimum velocity value at the undershoot was shifted to the right, towards the positive  $x$ -direction, with decreasing cellulose concentration. To investigate the possible effects of velocity on the undershoot, the next set of results was obtained using constant velocity at the beginning of the channel.

### Constant Initial Velocity Experiments

Because the addition of cellulose decreased foam velocity up to a factor of ten in the pressure controlled experiment, the second measurement set was performed with a constant initial velocity to eliminate rate dependent effects.



**Fig. 3.** a) The plot shows the  $u$ -component of velocity profiles at the center line  $y = 80$  mm. The curves depict four different cellulose concentrations as indicated by the legend. b) Scaling by the peak velocity  $u_{\max}$  collapsed the profiles.

In Fig. 4a, the velocity profiles at the center line were drawn for three cellulose concentrations. In this case, the initial values were exactly the same compared to the pressure controlled experiments. However, the peak value of velocity  $u_{\max}$  clearly fell as the value for  $C$  increased. In all cases, the undershoot was clearly visible and the minimum velocities were nearly the same for the different values of  $C$ . In the  $C = 0$  case, the velocity recovered its initial value faster than in the other cases. This is seen in Fig. 4a when  $x > 150$  mm, where the velocity displayed a clear gap between  $C = 0$  wt% and the rest of the curves.

The velocities scaled with peak velocity are plotted in Fig. 4 b. Due to the different  $u_{\max}$  values, the initial velocities no longer overlapped. In contrast to the present pressure controlled experiments, and earlier studies (Jones and Cox 2012; Langlois 2014) the collapse of the velocity curves was lost. Figure 4b reveals that compared to the peak

velocity, the undershoot was actually the largest when no cellulose was added. This might seem somewhat counterintuitive, because mixing a highly viscoelastic nanocellulose suspension and foam decreased the observed overshoot instead of increasing the overshoot. One possible explanation for this result was that the addition of cellulose increased the viscosity of the liquid films of the foam, which increased the dissipation, while the influence on the foam elasticity remained modest.

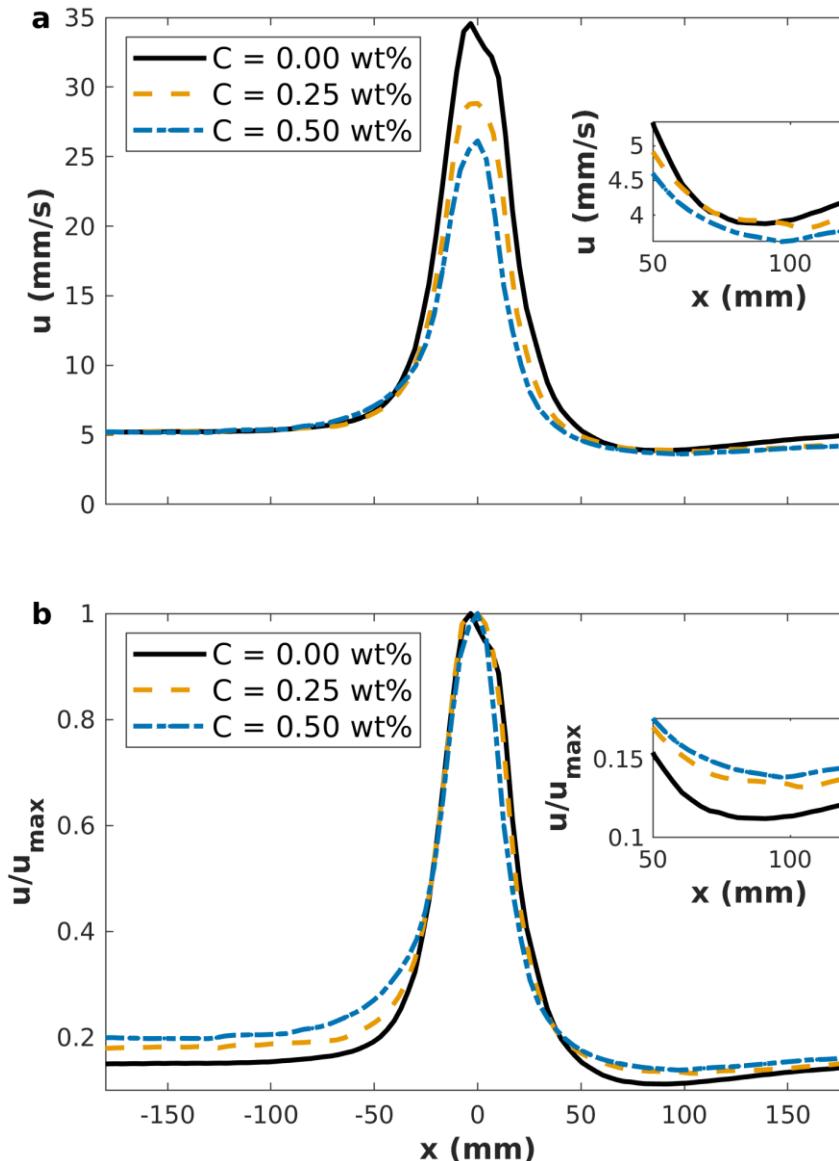


**Fig. 4.** a) The velocity  $x$ -component was plotted on an axis that passed through the constriction at  $y = 80$  mm. Each curve represents velocity measured with different cellulose concentration  $C$ . After the constriction, all curves dropped below the initial value  $u_0 = 5$  mm/s as shown in the inset. b) The plot shows the measurements depicted in Fig. 4a with the velocities scaled with the peak velocity  $u_{max}$ .

### Numerical Simulations

To both lend credence to and support the experimental observations presented in this work, numerical simulations were conducted in the continuum limit *via* utilizing the

full Navier-Stokes equations with the constitutive (viscoelastic) Giesekus model. The former established a relation among the foam velocity  $v$  and pressure  $p$ , while the latter contained the separable constitutive stress relations for the carrier fluid and bubbles ( $T_s + T_p$ ). The Giesekus model is common and also appropriate for the current study due to its simple formulation and numerical stability.

The subsequent set of equations was then discretized in the Finite Volume Method (FVM) framework, where the flow geometry was a Hele-Shaw cell, the dimensions of which were exactly matched to those of the experimental one, as described above (see Fig. 1). Explicitly stated, the equations read (Larson 1992; Baaijens 1998),

$$\nabla \cdot v = 0 \quad (3)$$

$$\frac{\partial v}{\partial t} + (v \cdot \nabla)v = -\nabla p + \nabla \cdot (T_s + T_p) \quad (4)$$

where the stress of the carrier fluid  $T_s$  is purely viscous with viscosity  $\eta_s$ . Additionally, the bubble contribution  $T_p$  has a similar viscous component with a different parameter  $\eta_p$ , and two additional terms. Of these, the first one describes the elastic deformation while the second one serves to constrain this deformation to a finite limit. These are depicted, respectively, in Eqs. 5 and 6:

$$T_s = 2\eta_s D \quad (5)$$

$$T_p = 2\eta_p D - \lambda T_p^{\nabla} - \frac{\alpha\lambda}{\eta_p} T^2 \quad (6)$$

In the above equations,  $D$  and  $T_p^{\nabla}$  are the standard strain rate tensor and upper convected derivatives, as defined by Eqs. 7 and 8, respectively,

$$T_p^{\nabla} = \frac{\partial T_p}{\partial t} + v \cdot \nabla T_p - (\nabla v)^T \cdot T_p - T_p \cdot \nabla v \quad (7)$$

$$D = 1/2(\nabla v + (\nabla v)^T) \quad (8)$$

where  $\alpha$  and  $\lambda$  are the model parameters;  $\alpha$  is typically obtained as a fitting parameter and  $\lambda$  is the fraction of the elastic and viscous time scales in the fluid. By setting  $\alpha = 0.9$ ,  $\lambda = 15.0$ , and  $\eta_p = 1$  Pas while varying  $\eta_s$ , a good agreement was obtained with the flow controlled experiments. The controlled flow rate was set to 5 mm/s as in the experiments presented in Figs. 4a and 4b.

While performing the simulations, it was assumed that increasing the NFC concentration in the experiments would be tantamount to increasing only the solvent viscosity  $\eta_s$  in the equations presented above, therefore enhancing the viscous energy dissipation in the computational model. This was quantified by defining the simulated concentration  $C_{\text{sim}} = \eta_s / \eta_p$ , which was altered by adjusting  $\eta_s$ . This proved to be a good approximation, as the results below adequately complied with the experiments.

These flow controlled simulations are displayed in Figs. 5a and 5b, exhibiting an anticipated behavior based on the experiments seen earlier in Figs. 4a and 4b. As in the experimental work, Fig. 5a displays the x-component of the simulated foam velocity along the center line of the Hele-Shaw cell, while Fig. 5b illustrates this component scaled by  $u_{\text{max}}$ . Figure 5a shows that increasing the concentration  $C_{\text{sim}}$  decreased the magnitude of the overshoot at the constriction, which was in agreement with the experimental results in Fig. 4a. Additionally, Fig. 5b indicates that lower values of  $C_{\text{sim}}$  corresponded to larger

undershoots past the constriction, which again complied with the experimental data in Fig. 4b. The absolute values of the overshoot and undershoot in Fig. 5a were somewhat different from the experimental results presented in Fig. 4a. However, this was remedied by fine-tuning the ratio of  $\alpha$  and  $\lambda$  to reflect the experimental foam system more accurately, as these two parameters had the most notable influence on the foam in the vicinity of the constriction. Because the model was not particularly designed to simulate particle laden foams, no attempts to perform such fine-tuning were made.

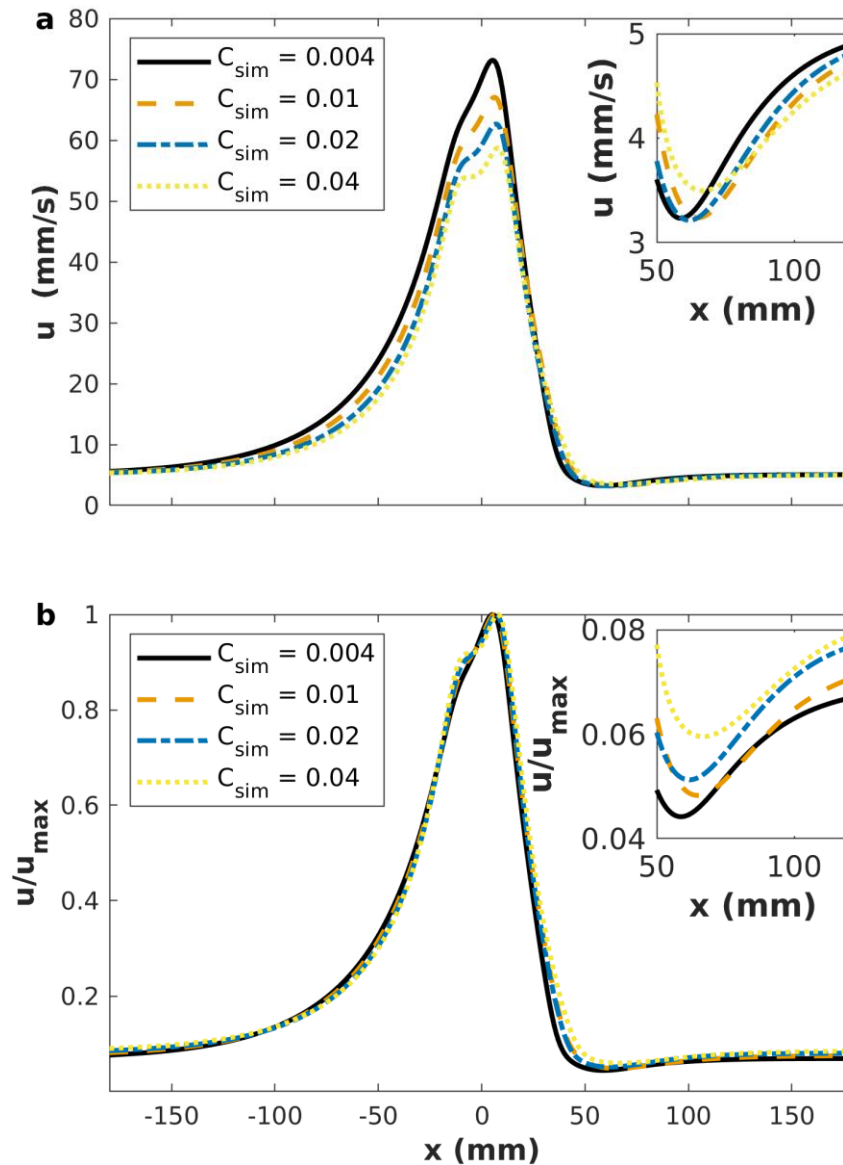


**Fig. 5.** a) The plot shows the simulated velocity profile  $x$ -component on the horizontal centerline. Each curve represents a simulation with different simulated cellulose concentration  $C_{sim}$ . The inset is zoomed in to the undershoot downstream of constriction. b) The plot shows the same simulation results as Fig. 5a except the velocities were scaled with the peak velocity  $u_{max}$ .

## CONCLUSIONS

1. Foam flow through a channel with a constriction displayed an undershoot, a typical viscoelastic response, after the constriction. The foams made of nanofibrillated cellulose suspension showed small changes in the flow field but the characteristic undershoot remained.
2. The overall flow resistance was increased *via* the addition of nanofibrillated cellulose as witnessed through the decrease of the peak velocity in the constant pressure experiments.
3. Nanofibrillated cellulose additives increased the effective viscosity of the foam. However, the foam damping (the relation of dissipation and elasticity) was not influenced by nanocellulose fibers, indicating the foam elasticity increased with an equal amount, as exemplified by the model. This will make it unnecessary to consider elastic recoil flows specifically related to nanocellulose additives in application environments.

## ACKNOWLEDGMENTS

The authors are grateful for the financial support of the Academy of Finland through projects 308235 and 278367. Professor Thaddeus Maloney (Department of Bioproducts and Biosystems, School of Chemical Engineering, Aalto University) for providing the microfibrillated cellulose. Aalto Science IT project is acknowledged for computational resources through Triton cluster. The authors are grateful for the support by the FinnCERES Materials Bioeconomy Ecosystem.

## REFERENCES CITED

- Alava, M., and Niskanen, K. (2006). "The physics of paper," *Reports on Progress in Physics* 69(3), 669. DOI: 10.1088/0034-4885/69/3/R03
- Baaijens, F. P. T. (1998). "Mixed finite element methods for viscoelastic flow analysis: A review," *Journal of Non-Newtonian Fluid Mechanics* 79(2-3), 361-385. DOI: 10.1016/S0377-0257(98)00122-0
- Chevalier, T., Koivisto, J., Shmakova, N., Alava, M. J., Puisto, A., Raufaste, C., and Santucci, S. (2017). "Foam flows through a local constriction," *Journal of Physics: Conference Series* 925(1), 1-6. DOI: 10.1088/1742-6596/925/1/012025
- Cohen-Addad, S., Höhler, R., and Pitois, O. (2013). "Flow in foams and flowing foams," *Annual Review of Fluid Mechanics* 45, 241-267. DOI: 10.1146/annurev-fluid-011212-140634
- Denkov, N. D., Tcholakova, S. S., Höhler, R., and Cohen-Addad, S. (2012). "Foam Rheology," in: *Foam Engineering: Fundamentals and Applications*, P. Stevenson (ed.), John Wiley & Sons, Chichester, UK, pp. 91-120.

- Dollet, B. (2010). "Local description of the two-dimensional flow of foam through a contraction," *Journal of Rheology* 54(4), 741-760. DOI: 10.1122/1.3380852
- Dollet, B., Elias, F., Quilliet, C., Raufaste, C., Aubouy, M., and Graner, F. (2005). "Two-dimensional flow of foam around an obstacle: Force measurements," *Physical Review E* 71(3), 031403. DOI: 10.1103/PhysRevE.71.031403
- Dollet, B., and Graner, F. (2007). "Two-dimensional flow of foam around a circular obstacle local measurements of elasticity, plasticity and flow," *Journal of Fluid Mechanics* 585, 181-211. DOI: 10.1017/S0022112007006830
- Gatward, A., and Radvan B. (1973). "Method and apparatus for forming a non-woven fibrous web from a foamed fiber furnish," U.S. Patent No. 3,716,449.
- Guillermic, R. M., Volland, S., Faure, S., Imbert, B., and Drenckhan-Andreatta, W. (2013). "Shaping complex fluids—How foams stand up for themselves," *Journal of Rheology* 57(1), 333-348. DOI: 10.1122/1.4769826
- Hassager, O. (1979). "Negative wake behind bubbles in non-Newtonian liquids," *Nature* 279(5712), 402-403. DOI: 10.1038/279402a0
- Jones, S. A., and Cox, S. J. (2012). "On the effectiveness of a quasistatic bubble-scale simulation in predicting the constriction flow of a two-dimensional foam," *Journal of Rheology* 56(3), 457-471. DOI: 10.1122/1.3687301
- Jones, S. A., Dollet, B., Slosse, N., Jiang, Y., Cox, S. J., and Graner, F. (2011). "Two-dimensional constriction flows of foams," *Colloids and Surfaces A: Physicochemical and Engineering Aspects* 382(1-3), 18-23. DOI: 10.1016/j.colsurfa.2010.11.054
- Katgert, G., and Van Hecke, M. (2010). "Jamming and geometry of two-dimensional foams," *Europhysics Letters* 92(3), Article ID 34002. DOI: 10.1209/0295-5075/92/34002
- Kiiskinen, H., Torniainen, E. and Kinnunen, K. (2016). "Method of forming a fibrous product," U.S. Patent Application 15/021,708.
- Kinnunen-Raudaskoski, K. (2017). "Foam as a carrier phase – A multipurpose technology for industrial applications," Ph.D. Dissertation, Aalto University, Helsinki, Finland.
- Koponen, A., Torvinen, K., Jäsberg, A., and Kiiskinen, H. (2016). "Foam forming of long fibers," *Nordic Pulp & Paper Research Journal* 31(2), 239-247. DOI: 10.3183/NPPRJ-2016-31-02-p239-247
- Langlois, V. J. (2014). "The two-dimensional flow of a foam through a constriction: Insights from the bubble model," *Journal of Rheology* 58(3), 799-818. DOI: 10.1122/1.4872058
- Lappalainen, T., Salminen, K., Kinnunen, K., Järvinen, M., Mira, I., and Andersson, M. (2014). "Foam forming revisited. Part II. Effect of surfactant on the properties of foam-formed paper products," *Nordic Pulp & Paper Research Journal* 29(4), 689-699. DOI: 10.3183/npprj-2014-29-04-p689-699.
- Larson, R. G. (1992). "Instabilities in viscoelastic flows," *Rheologica Acta* 31(3), 213-263. DOI: 10.1007/BF00366504
- Liu, A. J., and Nagel, S. R. (1998). "Nonlinear dynamics: Jamming is not just cool anymore," *Nature* 396(6706), 21-22.
- Møller, P. C., Mewis, J., and Bonn, D. (2006). "Yield stress and thixotropy: On the difficulty of measuring yield stresses in practice," *Soft Matter* 2(4), 274-283. DOI: 10.1039/B517840A

- O'Hern, C. S., Silbert, L. E., Liu, A. J., and Nagel, S. R. (2003). "Jamming at zero temperature and zero applied stress: The epitome of disorder," *Physical Review E* 68(1), 011306. DOI: 10.1103/PhysRevE.68.011306
- Puisto, A., Illa, X., Mohtaschemi, M., and Alava, M., (2012). "Modeling the rheology of nanocellulose suspensions," *Nordic Pulp & Paper Research Journal* 27(2), 277-281. DOI: 10.3183/npprj-2012-27-02-p277-281
- Al-Qararah, A. M., Ekman, A., Hjelt, T., Ketoja, J. A., Kiiskinen, H., Koponen, A., and Timonen, J. (2015). "A unique microstructure of the fiber networks deposited from foam-fiber suspensions," *Colloids and Surfaces A: Physicochemical and Engineering Aspects* 482, 544-553. DOI: 10.1016/j.colsurfa.2015.07.010
- Raufaste, C., Dollet, B., Cox, S., Jiang, Y., and Graner, F. (2007). "Yield drag in a two-dimensional foam flow around a circular obstacle: Effect of liquid fraction," *The European Physical Journal E* 23(2), 217-228. DOI: 10.1140/epje/i2006-10178-9
- Raufaste, C., Dollet, B., Mader, K., Santucci, S., and Mokso, R. (2015). "Three-dimensional foam flow resolved by fast X-ray tomographic microscopy," *Europhysics Letters* 111(3), Article ID 38004. DOI: 10.1209/0295-5075/111/38004
- Saint-Jalmes, A., and Durian, D. J. (1999). "Vanishing elasticity for wet foams: Equivalence with emulsions and role of polydispersity," *Journal of Rheology* 43(6), 1411-1422. DOI: 10.1122/1.551052
- Thielicke, W., and Stamhuis, E. (2014). "PIVlab—towards user-friendly, affordable and accurate digital particle image velocimetry in MATLAB," *Journal of Open Research Software* 2(1), e30-e39. DOI: 10.5334/jors.bl
- Torniainen, E., Mustonen, T., Kinnunen, K. and Hjelt, T. (2017). "Fiber sheets and structures comprising fiber sheets," U.S. Patent Application 15/529,142.
- Van Hecke, M. (2009). "Jamming of soft particles: Geometry, mechanics, scaling and isotaticity," *Journal of Physics: Condensed Matter* 22(3), Article ID 033101. DOI: 10.1088/0953-8984/22/3/033101

Article submitted: February 1, 2019; Peer review completed: April 17, 2019; Revised version received: May 5, 2019; Accepted: May 6, 2019; Published: June 3, 2019.

DOI: 10.15376/biores.14.3.5716-5728